Tuning the slow magnetic relaxation with the substituents in anilate bridged bis(dysprosium) complexes

Fabio Manna, Mariangela Oggianu, José Ramón Galán-Mascarós, Flavia Pop, Boris Le Guennic, Maria Laura Mercuri, N. Avarvari

Tuning the slow magnetic relaxation with the substituents in anilate bridged bis(dysprosium) complexes†

Fabio Manna,[a,b,c] Mariangela Oggianu,[a,c] José Ramón Galán-Mascarós,[d,e] Flavia Pop,[b] Boris Le Guennic,[f] Maria Laura Mercuri[a,c]* and Narcis Avarvari[b]*

[a]*Dipartimento di Scienze Chimiche e Geologiche, Università degli Studi di Cagliari, I-09042 Monserrato, Italy. E-mail: mercuri@unica.it*

[b] *Univ Angers, CNRS, MOLTECH-ANJOU, SFR MATRIX, F-49000 Angers, France. E-mail: narcis.avarvari@univ-angers.fr*

[c] *INSTM, Via Giuseppe Giusti, 9, 50121 Firenze, Italy*

[d]*Institute of Chemical Research of Catalonia (ICIQ), The Barcelona Institute of Science and Technology (BIST), Av. Països Catalans 16, E-43007 Tarragona, Spain*

[e]*ICREA, Passeig Lluis Companys, 23, Barcelona 08010, Spain*

[f] *Univ Rennes, CNRS, ISCR (Institut des Sciences Chimiques de Rennes) – UMR 6226, F-35000 Rennes, France*

†Electronic supplementary information (ESI) available: Figures S1-S24, Tables S1-S4. CCDC reference number 2324974–2324975. For ESI and crystallographic data in CIF or other electronic format see DOI: 10.1039/xxxxx.

Table of Contents Entry

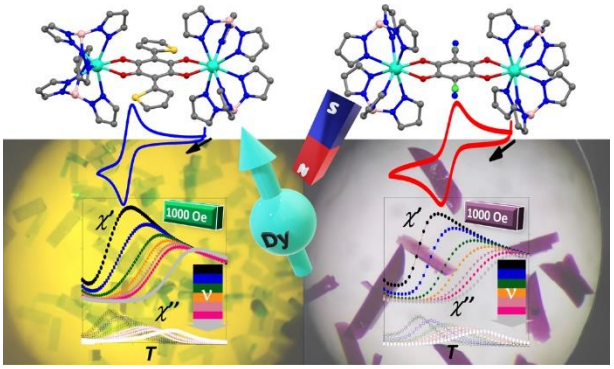

By combining homosubstituted dithiophene- and heterosubstituted chlorocyano-anilate bridging linkers, with the Dy^{III} ion and the scorpionate capping ligand, dinuclear Dy-complexes have been obtained, showing tunable SMM behavior thanks to the substituents at the 3,6 positions of the anilate moiety.

Abstract

Dinuclear lanthanide complexes [((HB(pz)$_3$)$_2$Dy)$_2$(μ-Th$_2$An)] **(1Dy)** and [((HB(pz)$_3$)$_2$Dy)$_2$(μ-ClCNAn)] **(2Dy)**, based on the hydrotris(pyrazol-1-yl)borate (HBpz$_3^-$) scorpionate capping ligand and anilate (An^{2-}) bridging linkers, namely homosubstituted dithiophene- and heterosubstituted chlorocyanoanilate, bearing electron-donating and withdrawing substituents at the 3,6-positions of the benzoquinone *core*, are reported. **1Dy** shows an octacoordinated {N$_6$O$_2$} Dy^{III} ion within a D$_{4h}$ distorted square antiprismatic coordination, an ideal geometry for Single-Molecule Magnet (SMM) behavior, given its oblate nature, whereas in **2Dy** the octacoordinated Dy^{III} ion adopts a D$_{2d}$ triangular dodecahedron geometry, while maintaining the same {N$_6$O$_2$} coordination sphere. Both complexes show field-induced single molecule magnet (SMM) behaviour, with tuning of the slow magnetic relaxation as a function of the nature of the substituents at the 3,6 positions of the anilate moiety. A comparison of the Arrhenius fitting parameters for **1Dy** and **2Dy** supports the hypothesis that square antiprismatic Dy^{III} complexes, as **1Dy**, exhibit higher energy barriers. This interpretation is supported by ab-initio calculations that also shed light on the crucial role of intermolecular dipolar interactions.

Introduction

Following the discovery of the so-called Single Molecule Magnet (SMM) behaviour in the Mn_{12} clusters, an intense activity has been continuously developed around this class of compounds motivated by their possible applications in new spintronic based devices.[1,2] Recently, several such materials were studied and particularly those based on Ln^{III} ions show promising properties. In this respect, Dy^{III} complexes are very interesting thanks to the strong magnetic moment and the Kramer nature of this ion.[3] Strategies focusing on the modulation of the coordination geometry around the Ln^{III} ion[4,5] that influences the crystal field, or on the suppression of relaxation pathways through strong exchange interactions between the Ln^{III} ions mediated by diamagnetic or paramagnetic ligands,[6–9] have been envisaged for inducing high energy barrier reversal of the magnetization. Quinone derivatives are well known in the field of coordination chemistry to be used as ligands in complexes ranging from 0D to polymeric species with intriguing magnetic, optical, and conducting properties.[10–13] Among quinone ligands, those based on 2,5-dihydroxy-1,4-benzoquinone (or anilic acid), referred to as anilates, can efficiently coordinate lanthanide and d-metal ions and, thanks to their non-innocent redox behaviour, allow a wide range of redox states[14,15] with fine tuning of the magnetic interactions.[16–21] Indeed, the anilate ligands can accommodate two subsequent mono-electronic redox processes, in the first one a semiquinone radical system being formed, that is generally stabilized by coordination, which can promote strong magnetic exchange interaction thanks to the open shell character.[22,23] Dinuclear lanthanide complexes based on the hydrotris(pyrazol-1-yl)borate ($HBpz_3^-$) scorpionate capping ligand and anilate (An) bridging linkers were first reported in 2004. [24] Here, 3,6-dichloroanilate (Cl_2An^{2-}) and scorpionate ($HBpz_3^-$) ligands were combined with the Tb^{III}, Er^{III} and Yb^{III} ions within dinuclear complexes that were studied for their luminescence properties, thus confirming the efficient antenna effect of anilate ligands towards NIR emitting Ln^{III} ions. Subsequently, several research groups further developed this promising system in the field of SMMs by using different Ln^{III} and anilate ligands motivated by the opportunity to fine tune the benzoquinone substituents in the 3,6 positions.[25] Accordingly, an intensive study on this family of compounds was made by Boskovic *et al.* in 2017, who reported different dinuclear complexes using combinations of eight rare earth (Re) ions (Re = Y, Eu, Gd, Tb, Dy, Ho, Er and Yb) and three anilate ligands beside the scorpionate, that is ($[(HBpz_3)_2Re_2(\mu\text{-}Cl_2An)]$, $[(HBpz_3)_2Re_2(\mu\text{-}H_2An)]$ and $[(HBpz_3)_2Re_2(\mu\text{-}Me_2An)]$)[26]. They succeeded as well to

obtain single crystals of dinuclear and tetranuclear complexes involving the $B(OMe)_4^-$ counter-ion formed *in situ* due to the scorpionate decomposition in MeOH. The study of the magnetic properties of $[(HBpz_3)_2Dy_2(\mu\text{-}Cl_2An)]$, $[(HBpz_3)_2Gd_2(\mu\text{-}Me_2An)]$, $[(HBpz_3)_2Tb_2(\mu\text{-}Me_2An)]$ and $[(HBpz_3)_2Dy_2(\mu\text{-}Me_2An)]$ showed slow relaxation for the Dy complexes. Unfortunately, the attempts to isolate the mono-reduced form, by chemical reduction in rigorously anaerobic and anhydrous conditions using cobaltocene ($CoCp_2$), through the formation of anilate radical anion were not successful during this first study. However, later on, the same group succeeded to isolate mono-reduced species of $[(HBpz_3)_2Re_2(\mu\text{-}Br_2An)]$ (Re = Y, Dy) using $CoCp_2$ in THF.[27] Magnetic data on the semiquinoid complex Dy_2 show relatively strong magnetic interactions and SMM behaviour in zero field, confirming the suppression of the quantum tunnelling of the magnetization induced by the paramagnetic bridging ligand. Only shortly before, the series $[CoCp_2][(HBpz_3)_2Ln(\mu\text{-}Cl_2An^{\bullet})Ln(HBpz_3)_2]$ (Ln = Dy, Tb, Gd, Y) containing the chloroanilate radical anion ligand was investigated by van Slageren *et al.*, who observed zero-field SMM behavior for Dy_2 and Tb_2 complexes.[28] Ishikawa *et al.* observed the field-induced slow magnetic relaxation for the Kramer ions Er^{III} and Yb^{III} in the corresponding bridged Cl_2An complexes.[29] We report herein the synthesis, crystal structures and magnetic properties of the novel $[((HB(pz)_3)_2Dy)_2(\mu\text{-}Th_2An)]$ **(1Dy)** (Th_2An = 3,6-dithiophene-anilate) and $[((HB(pz)_3)_2Dy)_2(\mu\text{-}ClCNAn)]$ **(2Dy)** (ClCNAn = 3-chloro-6-cyano-anilate) dinuclear Dy^{III} complexes, with the aim to investigate the influence of electronically different substituents at the 3,6 positions of the benzoquinone *core*, namely thiophene and Cl/CN respectively, on the SMM behaviour of the related complexes. Theoretical calculations support the experimental magnetic behaviour and shed light on the interplay between intra- and intermolecular magnetic interactions.

Results and discussion

Synthesis & characterization

2,5-dihydroxy-3,6-bis(thiophene-2-yl)-cyclohexa-2,5- diene-1,4-dione or dithiophene-anilic acid (H_2th_2An) is an anilate derivative reported by some of us and used as ligand in a preliminary report to generate a mononuclear square planar heteroleptic Cu^{II} complex with a 2,2-bipyridine co-ligand. [30] In the present study we have slightly modified the synthesis of the ligand and adapted it to gram scale, by using less amount of Pd catalyst and solvents. The Stille coupling

was conducted on 2,6-dibromo-3,4-dimethoxy-1,4-benzoquinone, a more accessible precursor than the diethoxy equivalent, that could be obtained in higher yields and with easier synthetic purification (Scheme 1). **1Dy** and **2Dy** were synthesized following the optimized method used by Boskovic *et al.*[31] for similar dinuclear Ln^{III} complexes with slight modifications. First, four equivalents of potassium tris-pyrazolylborate ($KHB(pz)_3$) have been reacted with two equivalents of Dy^{III} salt in dichloromethane (CH_2Cl_2) / ethanol (EtOH) mixture and then a solution of one equivalent of H_2th_2An doubly deprotonated with triethylamine (TEA) in CH_2Cl_2 has been added for the synthesis of $[((HB(pz)_3)_2Dy)_2(\mu\text{-}Th_2An)]$ **(1Dy)**. Alternatively, a suspension of monopotassium salt of clorocyanoanilate (KHClCNAn) in CH_2Cl_2/EtOH mixture with two equivalents of TEA has been used for the synthesis of $[((HB(pz)_3)_2Dy)_2(\mu\text{-}ClCNAn)]$ **(2Dy)**. X-ray quality crystals were grown for both complexes, for **1Dy** the yield being very high (95%) compared to **2Dy** (45%), very likely due to the lower solubility of the ClCNAn ligand and of the corresponding complex. Indeed, during the synthesis, a thin white solid, which was filtered before crystallization, was formed in the reaction mixture. The amount of this precipitate was much higher for **2Dy** and also unreacted ligand was present. During the attempts to improve the yield of **2Dy**, by decreasing reagents concentrations or by recrystallization in other mixtures of solvents (mixtures containing THF and DCM were complexes are well soluble), we obtained however the same yield and white impurities solids still formed. **1Dy** shows fast solvent loss after filtration and thus the phase purity could be checked by powder X-ray diffraction (PXRD) analysis on a gently grinded freshly filtered sample (Fig. S1). The easy room temperature (RT) desolvation was confirmed also by TGA analysis, which indicates no crystallization solvent loss up to 200 °C (Fig. S2), while the elemental analysis matches with the fully desolvated form of the complex. On the contrary, **2Dy** does show gradual solvent loss between RT and 200 °C. However, both complexes are stable up to 200 °C, temperature after which decomposition occurs (Fig. S2). Furthermore, stability in solution and in the solid state was confirmed by ESI and MALDI mass spectrometry measurements for both complexes.

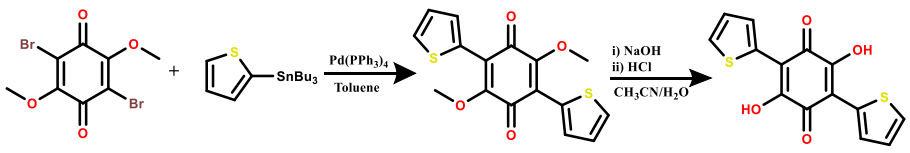

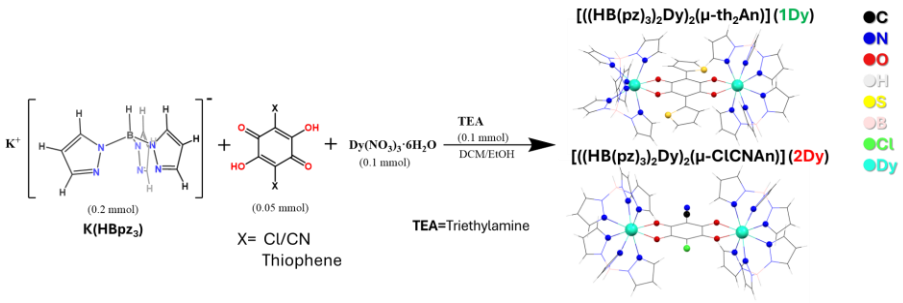

Scheme 1 Synthesis of 2,5-dihydroxy-3,6-bis(thiophene-2-yl)-cyclohexa-2,5-diene-1,4-dione (H_2th_2An) (top). Synthesis of complexes **1Dy** and **2Dy** (bottom).

Crystal structures

Compound **1Dy** crystallizes as green rectangular prisms (Fig. S3) in the tetragonal centrosymmetric $P4_2/n$ space group with half a complex and two CH_2Cl_2 molecules per asymmetric unit (Fig. 1). Four $HB(pz)_3^-$ chelating ligands coordinate the two Dy^{III} and each lanthanide is coordinated by six N atoms from the pyrazolyl groups.

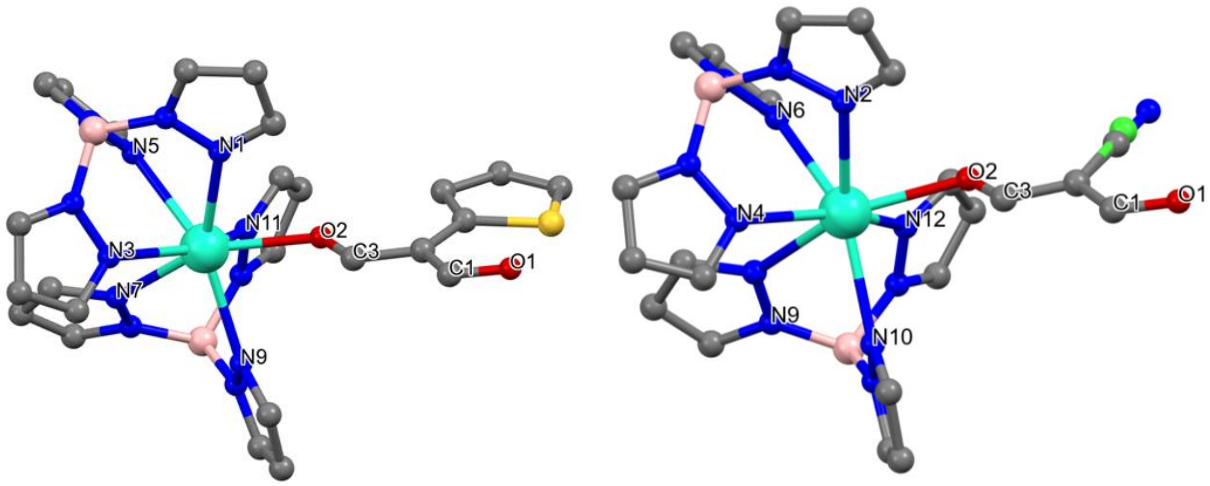

Fig. 1 Ball and stick representation of the asymmetric unit for **1Dy** (left) and **2Dy** (right). Colour code: C, grey; N, blue; O, red; B, pink; S, yellow; Cl, green; Dy, turquoise. Hydrogen atoms and solvent molecules have been omitted for clarity.

The coordination sphere of each metal is completed by two oxygen atoms from the doubly deprotonated anilato bridging ligand, thus leading to a neutral dimeric complex. This provides an octacoordinated $\{N_6O_2\}$ Dy^{III} ion within a D_{4h} distorted square antiprismatic coordination (Fig. 2), as confirmed by continuous shape measurement (CShM) performed with the software

Shape2.1.[32,33] The C–O distances of 1.259(4) Å and 1.258(4) Å are confirming the delocalized character of the anilate ligand, while the Dy–O distances of 2.349(2) Å and 2.339(2) Å, and the Dy–N distances ranging between 2.430 Å and 2.516 Å (Table 1), are similar to the reported values for this family of dimeric lanthanide complexes.[24–29] This geometry is particularly suitable for Dy-SMMs due to the oblate nature of this ion.[4] The Dy···Dy intramolecular distance is 8.593 Å and the shortest intermolecular one is 8.038 Å. The presence of open channels filled by volatile solvent molecules could be an explanation of the fast collapse of the structure due to solvent loss (Fig. S4-S5). Interestingly, no disorder due to free rotation of the thiophene rings was detected.

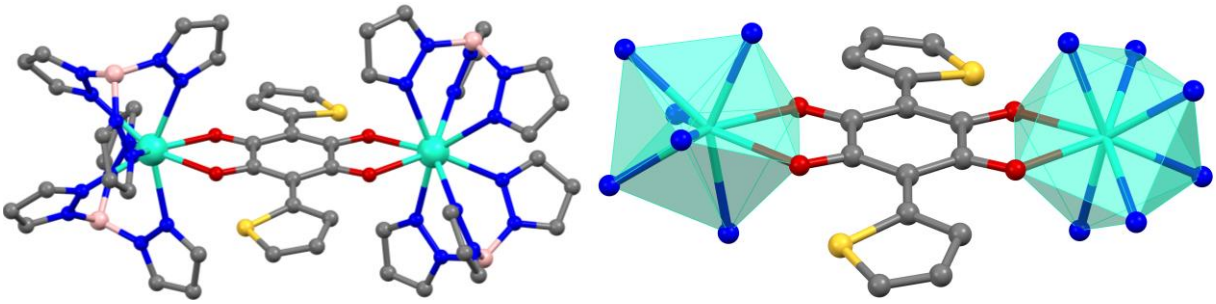

Fig. 2 Ball and stick representation of **1Dy** (left) together with the polyhedral representation that emphasizes the coordination geometry around Dy^{III} (right). Colour code: C, grey; N, blue; O, red; B, pink; S, yellow; Cl, green; Dy, turquoise. Hydrogen atoms and solvent molecules have been omitted for clarity.

The compound **2Dy** crystallizes as purple prisms (Fig. S6) in the centrosymmetric monoclinic $P2_1/n$ space group with half a complex and one CH_2Cl_2 molecule per asymmetric unit (Fig. 1, *vide supra*). The structure is isomorphous to the dinuclear complexes with Ln^{III} ions which crystallize in the same space group and show the same solvation pattern.[26] The centrosymmetric character is maintained even if the asymmetric chlorocyananilato ligand was used as bridging ligand. Indeed, the Cl/CN substituents are equally distributed in the structure due to the 0.5 partial occupancy in the asymmetric unit, this feature being common for compounds involving the $ClCNAn^{2-}$ ligand.[16] The octacoordinated Dy^{III} has the same coordination sphere $\{N_6O_2\}$ but with a different geometry suggested by CShM. It adopts indeed a D_{2d} triangular dodecahedron geometry (Fig. 3), similar to other isomorphous compounds.[26,27] The C–O distances are slightly shorter, i.e. 1.248(4) Å and 1.250(4) Å, and the Dy–O slightly longer, 2.377(2) Å and 2.379(2) Å (Table 1), probably due to the presence of the electron withdrawing cyano group on the benzoquinone ligand. The Dy–N distances are between 2.543 Å and 2.423 Å, similar to **1Dy**, while the intramolecular and shortest

intermolecular Dy···Dy distances are slightly longer, i.e. 8.659 Å and 8.667 Å, due to the different packing (Fig. S7-S9) and nature of the anilate ligand.

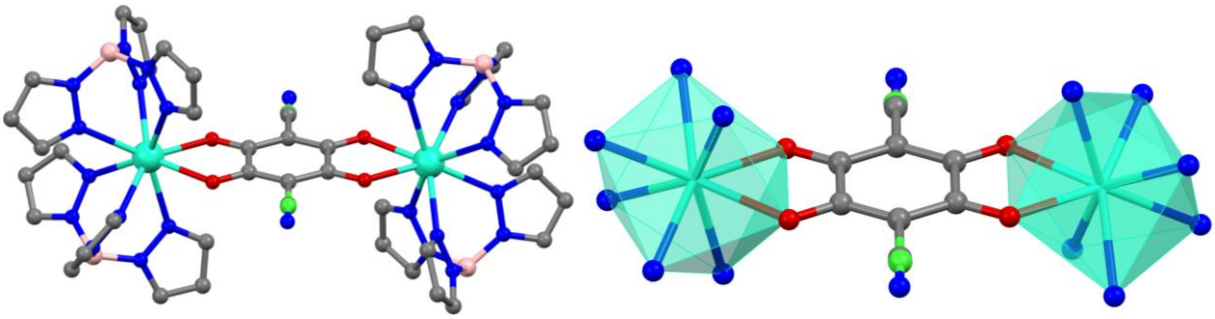

Fig. 3 Ball and stick representation of **2Dy** (left) together with the polyhedral representation that emphasizes the coordination geometry around Dy^{III} (right). Colour code: C, grey; N, blue; O, red; B, pink; S, yellow; Cl, green; Dy, turquoise. Hydrogen atoms and solvent molecules have been omitted for clarity.

Table 1 Selected bond distances and continuous shape analysis for 1Dy and 2Dy.

Selected bond distances **1Dy** (Å)	Selected bond distances **2Dy** (Å)
C-O	**C-O**
C1-O1 1.259(4)	C1-O1 1.248(4)
C3-O2 1.258(4)	C3-O2 1.250(4)
Dy-O	**Dy-O**
Dy-O1 2.349(2)	Dy-O1 2.377(2)
Dy-O2 2.339(2)	Dy-O1 2.379(2)
Dy-N	**Dy-N**
Dy-N1 2.499(3)	Dy-N2 2.543(2)
Dy-N3 2.455(3)	Dy-N4 2.423(3)
Dy-N5 2.503(3)	Dy-N6 2.448(3)
Dy-N7 2.485(3)	Dy-N8 2.509(2)
Dy-N9 2.516(3)	Dy-N10 2.508(2)
Dy-N11 2.430(3)	Dy-N12 2.464(3)
Dy···Dy	**Dy···Dy**
intramolecular 8.593	intramolecular 8.659
intermolecular 8.038*	intermolecular 8.667*

CShM parameter (Shape2.1) parameter **1Dy**	CShM parameter (Shape2.1) parameter **2Dy**
SAPR-8 D_{4d} 1.861	TDD-8 D_{2d} 2.442
BTPR-8 C_{2v} 2.233	JBTPR-8 C_{2v} 3.331
	SAPR-8 4.871
SAPR-8 (square antiprism), BTPR-8 (biaugmented trigonal prism), TDD-8 (triangular dodecahedron), JBTPR-8 (biaugmented trigonal prism J50). *Intermolecular lowest distances between two Dy of different complexes.	

Regarding the accessibility to the semiquinone form of the complexes, the presence of electrodonating/withdrawing groups as thiophene or cyano should decrease/increase respectively the reduction potentials (*vide infra*).

IR spectroscopy and UV-Vis spectroscopy

The infrared spectra of **1Dy** and **2Dy** were measured with an ATR set-up in the 400-4000 cm^{-1} range for the complexes and the ligands (Fig. S10-S11). The spectra for both complexes exhibit characteristic vibrational modes attributed to the B–H stretch of $HB(pz)_3^-$ around 2450 cm^{-1}, confirming the presence of the coordinated scorpionate ligand. Characteristic ν_{CO} stretch bands attributed to the carbonyl of anilate ligands are present around 1500 cm^{-1} in both complexes, thus shifted to lower energy with respect to the ligand alone (1600 cm^{-1}), due to the coordination of Dy^{III}. The stronger frequency shift to lower energy in the case of **1Dy** (1496 cm^{-1}) compared to **2Dy** (1542 cm^{-1}) is likely due to the electron donating character of the thiophene substituent. Furthermore, **2Dy** shows the characteristic band of the CN substituent at 2223 cm^{-1}, the fingerprint regions being similar for both complexes confirming similar coordination modes.[26,31] UV-Vis absorption measurements in the 220-800 nm range were performed for both compounds in CH_2Cl_2 solutions (Fig. S12). **1Dy** shows strong bands in the UV-Vis region around 230 – 350 nm that are attributed the π-π^* transitions of the benzoquinone moiety.[26,30] The absorption at 433 nm is due to a charge transfer transition involving the thiophene and benzoquinone moieties, this being highly red shifted compared to the protected ligand alone. Furthermore, the broad band in the visible range with low extinction coefficient centred at around 700 nm can be attributed to a n-π* transition involving the anilate ligand. **2Dy** shows similar characteristic π-π^* transitions around 230 – 350 nm, while the n-π* band in the visible range with low extinction coefficient is centred

around 540 nm, giving an explanation to the strong difference in colour: green for **1Dy** and purple for **2Dy**.

Electrochemistry

The redox behaviour of the two complexes and of the ligands was studied to have information of the reduction processes involving the benzoquinone moiety, that could show in principle two single electron reduction processes from quinone to radical semiquinone anion and then to dianionic form (Fig. 4).

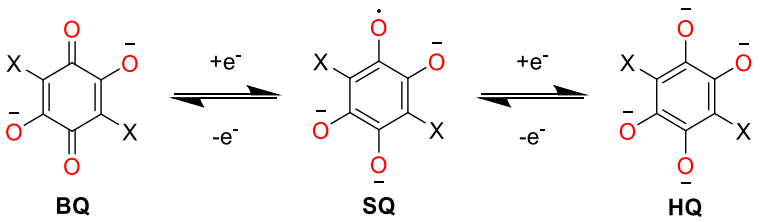

Fig. 4 Redox processes of fully deprotonated anilate ligands. BQ = benzoquinone; SQ = semiquinone; HQ = hydroquinone.

The experiments were performed with a three-electrode set-up at 298 K in a N_2 filled glovebox in degassed and dry 0.05 mM solution in CH_2Cl_2 or CH_3CN (used for KHClCNAn due to solubility), $TBAPF_6$ 0.25 M as supporting electrolyte. The potential was corrected and reported against the Ferrocene/Ferrocenium ($Fc^{0/+}$) couple, which was used as internal reference. The results are summarized in Fig. 5 and Table 2. As well documented, the semiquinone form can be stabilized by complexation of metal ions. Indeed, for the ligand alone two irreversible reduction processes are present (Fig. S13-S14), but for **1Dy** the first one (**I**) is reversible and for **2Dy** quasi-reversible (Fig. 5). **1Dy** shows the mono-reduction reversible peak at $E_{1/2}$ = -1.14 V, shifted at lower potential with respect to the halogen substituted anilate, due to the electron donating thiophene group. The I_{pa}/I_{pc} ratio is close to 1, proving the reversibility of the process and the stability of the radical species. A second irreversible reduction peak, attributed to the formation of the tetraanion[28] is present at -2.13 V (Fig. 5). The oxidation peaks at 0.66 V and 1.11 V can be assigned to the oxidation of the thiophene and the benzoquinone groups, respectively (Fig. S15). **2Dy** shows a similar behaviour, yet a larger peak separation is observed and the I_{pa}/I_{pc} ratio indicates a quasi-reversible reduction peak to semiquinone centred at -0.86 V. The second reduction process is

irreversible and occurs at -1.84 V (Fig. 5), while the irreversible oxidation takes place at 1.54 V (Fig. S15). The anodic shifts of the two reduction processes when compared to **1Dy** are due to the electron withdrawing CN group. Both complexes seem suitable for one electron reduction with cobaltocene ($CoCp_2$) using the method reported by Van Slageren et al., [31]since the $CoCp_2/CoCp_2^+$ potential ($E_{1/2}$ = -1.33 V)[34] is between the two reduction processes of our Dy compounds.

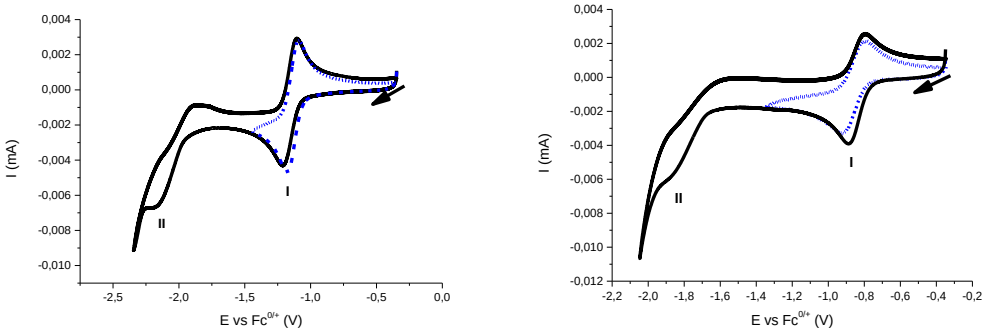

Fig. 5 Cyclic voltammograms for **1Dy** (left) and **2Dy** (right) in the cathodic region highlighting the two reduction processes (**I** & **II**); the dashed blue lines plots show the voltammograms measured with a switching potential immediately past the first reduction to probe the reversibility. Working conditions: platinum disk 2 mm (WE), platinum wire (CE), Ag wire (RE), $TBAPF_6$ 0.25 M in CH_2Cl_2 as electrolyte and 0.005 M complex concentration at 298 K in a N_2 filled glove box and referenced against the $Fc^{0/+}$ couple. The arrows indicate the direction of forwarded scan.

Table 2 E_p $E_{1/2}$/V (ΔE_p/mV) for Th_2An, KHClCNAn, 1Dy and 2Dy.						
Compound	$E_{1/2}$(**I**)/V (ΔE_p/mV)	i_{pa}/i_{pc}	E_{pc}(**I**)/V	E_{pc}(**II**)/V	E_{pa}(**III**)/V	E_{pa}(**IV**)/V
th_2An			-0.74	-1.52	0.92	
KHClCNAn			-1.13	-1.88	0.90	
1Dy	-1.14 (82)	0.99	-1.18	-2.13	0.66	1.11
2Dy	-0.86 (120)	0.93	-0.92	-1.84	1.54	

Magnetic properties

The thermal dependence of the dc magnetic data shows $\chi_m T$ values at room temperature of 27.50 and 26.31 emu·K·mol^{-1} for **1Dy** and **2Dy**, respectively, which are in good agreement with the theoretical value of ≈ 14,17 emu·K·mol^{-1} per Dy^{III} ion in a free-ion approximation ($4f^9$, J =

15/2). Upon cooling, the $\chi_m T$ products decrease slowly to reach values of 24.92 and 22.60 emu K mol^{-1} at 2 K, respectively (Fig. 6). This behavior can be assigned to the thermal depopulation of the M_J sublevels of the ground state splitted by crystal field effects. There is no apparent evidence of intermolecular magnetic interactions in these data, yet the situation is more complex according to the theoretical calculations (*vide infra*).

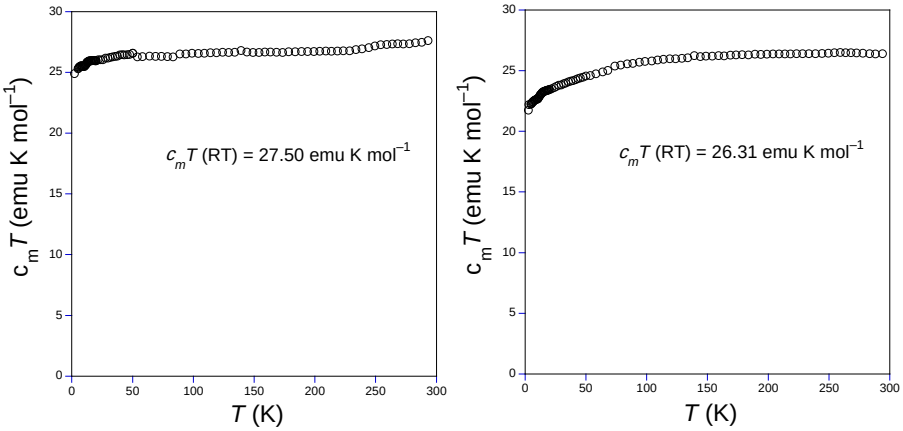

Fig. 6 Thermal dependence of the $\chi_m T$ product for **1Dy** (left) and **2Dy** (right) at 1000 Oe.

Alternating current (ac) magnetic susceptibility data were measured in the temperature range 2–15 K. The compounds do not exhibit an appreciable out-of-phase (χ'') signal in the absence of an applied magnetic field (Fig. S16), suggesting rapid quantum tunneling of the magnetization. We found that a static dc field (H = 1000 Oe) is able to suppress the tunneling processes, with the appearance of an out-of-phase signal with a strong dependence on the frequency of the ac field in the 10–10000 Hz range (Fig. 7-8).

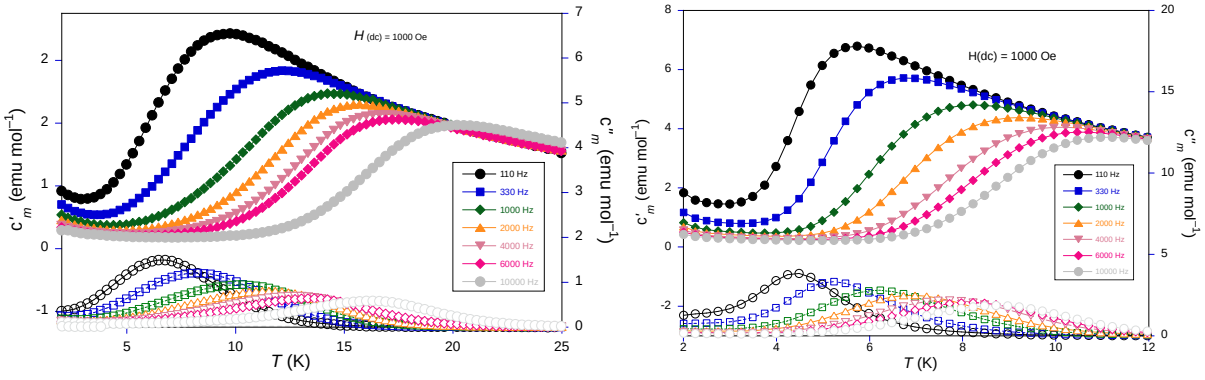

Fig. 7 Frequency dependence of the in-phase (top) and out-of-phase (bottom) ac magnetic susceptibility as a function of temperature in the range 10–10000 Hz range performed with an applied field of 1000 Oe for **1Dy** (left) and **2Dy** (right).

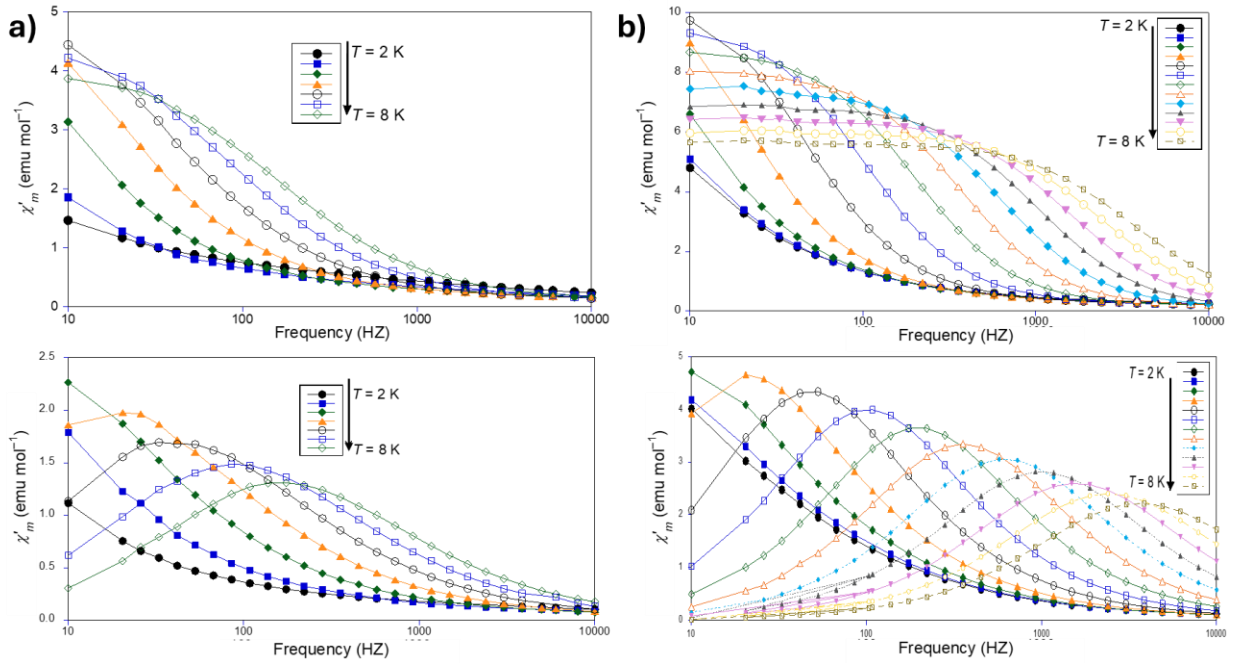

Fig. 8 Temperature dependence of the in-phase (top) and out-of-phase (bottom) ac magnetic susceptibility as a function of frequency (v) in the 10–10000 Hz range performed with an applied field of 1000 Oe for **1Dy** (panels a) and **2Dy** (panels b). Some frequencies were omitted for clarity.

χ'' appears below 20 K for **1Dy** but below 12 K for **2Dy**, suggesting stronger single ion anisotropy in the former. Accordingly, Arrhenius fits of the temperature-dependent relaxation time allows to estimate activation barriers of 47 and 37 K (Fig. 9) and τ_0 = 7.6 x 10^{-6} s and 2.61 x 10^{-6} s respectively.

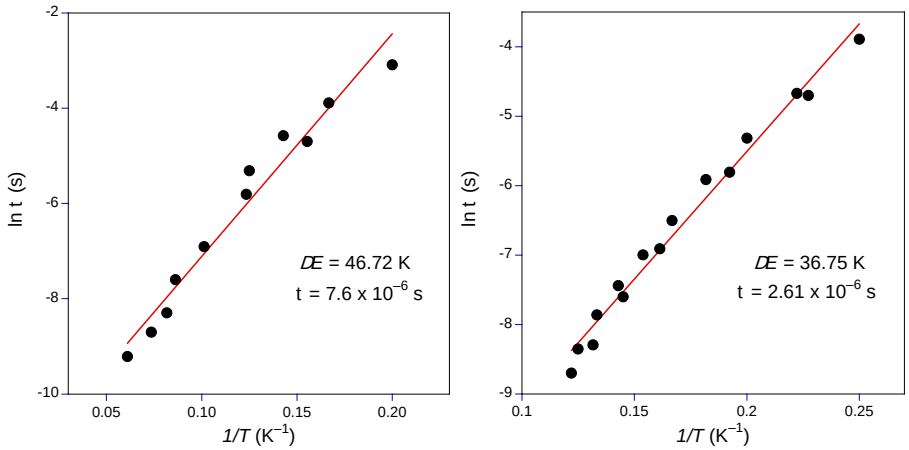

Fig. 9 Plots of ln τ versus T^{-1} for **1Dy** (left) and **2Dy** (right) in 1000 Oe dc fields. The solid lines correspond to the Arrhenius fit considering single relaxation process.

These parameters show typical values when compared with other SMM belonging to the family of bis(dysprosium) bridged tetraoxolene complexes.[25–28] The Argand plots obtained for the χ_m'' vs χ_m' plots show single, regular semicircles in a large temperature range, with small α parameters of 0.26 and 0.16, supporting the single relaxation process at the origin of the SMM behavior observed in these compounds (Fig. S17). A comparison of the Arrhenius fitting parameters for this family of complexes is given in Table 3. The comparison supports the hypothesis that square antiprismatic (SAPR) Dy complexes, as the case of **1Dy**, exhibit higher energy barriers. As briefly discussed in the Introduction, similar binuclear complexes with various Ln^{III} ions and anilate ligands were reported in the literature, and their magnetic properties were studied through *ac* magnetic measurements. For example, investigations on a Tb^{III} complex of this family, namely $[((HB(pz)_3)_2Tb)_2(\mu\text{-}Me_2An)]$, did not show any evidence of SMM properties even under applied field.[26] However, later on, slow relaxation of the magnetization was reported for the Tb^{III} reduced compound $[CoCp][((HB(pz)_3)_2Tb)_2(\mu\text{-}Cl_2An^{\bullet})]$, containing the bridging ligand as radical anion.[28] In this case, an out of phase signal was detected with zero field, suggesting an improvement of the SMM properties compared to the neutral counterpart, although the process was too fast to determine the energy barrier. This can easily be understood thanks to the study of Ishikawa *et al.* where *ac* susceptibility was measured for the series $[((HB(pz)_3)_2Ln)_2(\mu\text{-}Cl_2An)]$ (Ln^{III} = Gd, Tb, Ho, Er, and Yb).[29] Intramolecular nuclear hyperfine coupling interactions, dipolar interactions, and transverse fields from the off-diagonal crystal field splitting are expected for this series and, therefore, application of a small *dc* field is necessary to suppress the QTM. Only the Kramers ions

Yb^{III} and Er^{III}, with prolate electron density, showed field induced slow magnetic relaxation that occurs through Orbach and Raman relaxation processes, with similar energy barrier values (Table 3). Nevertheless, the relaxation dynamics is different with respect to the isostructural Dy complex, having the same triangular dodecahedron (TDD) coordination geometry.

Table 3 Comparison between dinuclear Dy complexes involving anilate ligands.

Formula	H_{dc} (Oe)	U_{eff} (K)	τ_0 (s)	Geometry	Ref.
$[((HB(pz)_3)_2Dy)_2(\mu\text{-}Cl_2An)]$	950	44,7	3.43×10^{-7}	TDD-8	[25]
$[((HB(pz)_3)_2Dy)_2(\mu\text{-}Cl_2An)]$	1000	39	5.46×10^{-6}	TDD-8	[28]
$[CoCp][((HB(pz)_3)_2Dy)_2(\mu\text{-}Cl_2An\cdot)]$	1600	31	7.33×10^{-9}	n.d.	[28]
$[((HB(pz)_3)_2Dy)_2(\mu\text{-}Cl_2An)]$	1600	24	3×10^{-5}	TDD-8	[26]
$[((HB(pz)_3)_2Dy)_2(\mu Me_2An)]$	1600	47	1.0×10^{-5}	SAPR-8*	[26]
$[((HB(pz)_3)_2Dy)_2(\mu\text{-}Br_2An)]$	390	7	1.4×10^{-4}	TDD-8	[27]
$[CoCp][((HB(pz)_3)_2Dy)_2(\mu\text{-}Br_2An\cdot)]$	0	10,4	9.6×10^{-8}	n.d.	[27]
$[CoCp][((HB(pz)_3)_2Dy)_2(\mu\text{-}Br_2An\cdot)]$	380	10,6	8.6×10^{-8}	n.d.	[27]
$[((HB(pz)_3)_2Dy)_2(\mu\text{-}Th_2An)]$	1000	46.7±0.5	$7.6\pm0.2 \times 10^{-6}$	SAPR-8	This work
$[((HB(pz)_3)_2Dy)_2(\mu\text{-}ClCNAn)]$	1000	36.8±0.3	$2.61\pm0.11 \times 10^{-6}$	TDD-8	This work
$[((HB(pz)_3)_2Er)_2(\mu\text{-}Cl_2An)]$	1000	25.9	3.04×10^{-9}	TDD-8	[29]
$[((HB(pz)_3)_2Yb)_2(\mu\text{-}Cl_2An)]$	1000	22.3	2.68×10^{-8}	TDD-8	[29]

*Geometry determined for Y compound, n.d.= non determined due to lack of crystal structure

Ab Initio Calculations

To investigate the magnetic properties of compounds **1Dy** and **2Dy**, theoretical calculations have been performed at the SA-CASSCF/RASSI-SO level for each inequivalent Dy^{III} center on the structures obtained by X-ray diffraction for which positions of hydrogen atoms have been optimized with DFT (Computational details in the Experimental Section). Let's first notice that the DFT computed Mülliken charges on the oxygen atoms reflect the less electron rich character of the anilate bridge in **2Dy** compare to **1Dy** (Cl/CN *versus* thiophene) with an average charge on oxygen of -0.675 and -0.706 for **2Dy** and **1Dy**, respectively. This slight change in the electrostatics

of the first coordination sphere of the Dy centres explains the observed differences in the magnetic properties of both complexes. Indeed, the overall splitting of the ground state multiplet of **1Dy** is about 610 cm^{-1} with the first excited Kramers doublet (KD) lying 120 cm^{-1} above the ground KD (Tables S1-S2), while the global splitting in **2Dy** is about 500 cm^{-1} with the first excited Kramers doublet (KD) lying 80 cm^{-1} above the ground KD (Tables S3-S4). More significantly, while the ground Kramers doublets are almost pure $m_j = |\pm 15/2\rangle$ for both compounds (99% for **1Dy** and 97% for **2Dy**), less axiality is found for **2Dy** ($g_x = 0.1$, $g_y = 0.1$, $g_z = 19.6$) compare to **1Dy** ($g_x = 0.0$, $g_y = 0.0$, $g_z = 19.8$). These behaviours are in line with the fact that **1Dy** behaves as a better in-field SMM than **2Dy** as confirmed by the computed magnetic transition moments (Fig. S20-S21) with faster QTM and TA-QTM processes in **2Dy**. Intramolecular Dy···Dy distances of about 8.5 Å preclude the presence of exchange coupling. However, as shown by the orientations of the magnetic anisotropy axes (Fig. S22 and S23 for **1Dy** and **2Dy**, respectively), one may expect intramolecular ferromagnetic dipolar coupling. This is confirmed by the intramolecular dipolar interactions that are calculated using the following equation:

$$E = \frac{\mu_0}{4\pi\vec{r}^3}\left[\vec{\mu}_1 \cdot \vec{\mu}_2 - \frac{3}{\vec{r}^2}(\vec{\mu}_1 \cdot \vec{r})(\vec{\mu}_2 \cdot \vec{r})\right]$$

with r the Dy–Dy vector, and μ_1 and μ_2 the magnetic moment vectors of the two Dy^{III} centres. The following Hamiltonian is employed:

$$H = -J_{dip}\tilde{S}_1\tilde{S}_2$$

with $\tilde{S}$ the pseudospin $\tilde{S} = 1/2$ operators at both dysprosium sites. The dipolar interaction is calculated slightly higher for **1Dy** (J_{dip} = 0.53 cm^{-1}) than for **2Dy** (J_{dip} = 0.49 cm^{-1}) again in line with the observed orientation of the magnetic axes. While the low-temperature experimental behaviour of the $\chi_m T$ *versus* T curve does not agree with these ferromagnetic interactions, explanation can only be found considering slight compensating anti-ferromagnetic interactions induced by the specific packing organizations and the intermolecular Dy···Dy distances in the same range as intramolecular ones (*vide supra*). This interpretation is supported, in the case of **2Dy**, by including small anti-ferromagnetic mean field zJ contributions (Fig. S24).

Conclusions

We have introduced in this work original homo- and heterosubstituted anilate ligands as efficient bridging ditopic chelating linkers towards Dy^{III} ions in $[((HB(pz)_3)_2Dy)_2(\mu\text{-}Th_2An)]$ **(1Dy)** and $[((HB(pz)_3)_2Dy)_2(\mu\text{-}ClCNAn)]$ **(2Dy)** dinuclear complexes, showing field-induced SMM properties. The nature of the anilate substituents, i.e. electron rich thiophene in **1Dy** *versus* electron poor Cl/CN in **2Dy**, plays a crucial role in triggering the coordination geometry around the lanthanide ion and the slow magnetic relaxation process. Accordingly, while in both compounds the metal ion is octacoordinated within a $\{N_6O_2\}$ environment, the coordination geometries are distorted square antiprismatic D_{4h} and triangular dodecahedron D_{2d} in **1Dy** and **2Dy**, respectively. The activation energy barriers of the relaxation process, determined by ac magnetic measurements on crystalline samples, show a significant difference in their values, i.e. 47 K (**1Dy**) and 37 K (**2Dy**), a modulation due to the different coordination geometry and, possibly, to the different electronic properties of the substituents (electron-donating *vs* electron withdrawing). Ab initio calculations explain the better SMM performance of 1Dy compared to 2Dy and highlight, for the first time in this family of lanthanide binuclear compounds, the existence of a dipolar Dy···Dy intramolecular ferromagnetic interaction which is compensated by intermolecular antiferromagnetic interactions. Noteworthy these results provide a challenging route to tune SMM properties in this family of dinuclear lanthanide complexes, by tailoring the substituents at the 3,6 positions of the anilate moiety, through conventional synthetic methods of organic and coordination chemistry. A rational study on several Dy-complexes is further needed to confirm these findings. These results also open the way towards the use of other lanthanide ions within dinuclear magnetic complexes with variable magnetic anisotropies. Moreover, the possibility to reduce the anilate bridge into semiquinone radical as a means to enhance the intramolecular magnetic exchange between the lanthanide ions is under active investigation with the aim to improve SMM properties.

Experimental

General Procedures

All manipulations were performed under aerobic conditions or under inert Ar atmosphere by using standard Schlenk line techniques and all chemicals purchased were of reagent grade or higher and used as received. 2,5-dibromo-3,6-dimethoxycyclohexa-2,5-diene-1,4-dione[35] and

KHClCnAn[31] were synthesized as previously reported; toluene was dried 24 h under Ar with 3 Å activated molecular sieves (15% m/V) and then filtered. Nuclear magnetic resonance spectra were recorded on a Bruker Avance DRX 300 spectrometer operating at 300 MHz for ^{1}H (Figures S18-S19). Chemical shifts are expressed in parts per million (ppm) downfield from external TMS. The following abbreviations (δ) are used: s, singlet; d, doublet. MALDI-TOF MS spectra were done on a Bruker Biflex-IIITM apparatus, equipped with a 337 nm N_2 laser, exact mass determination on a Spiral-TOF Jeol JMS3000 and a Bruker Esquire 3000 plus spectrometer was used for electrospray ionization mass spectrometry (ESI-MS). The IR spectra were performed on an ATR Bruker Vertex 70 spectrophotometer in the range 4000–400 cm^{-1}. UV–vis absorption spectra were recorded using Shimadzu UV 1800 in the range 220-800 nm in CH_2Cl_2 solutions. TGA Q500 from TA Instruments was used for TGA measurements under a nitrogen flow of 40 $mL \cdot min^{-1}$ at atmospheric pressure in the temperature range 25 – 800 °C at a heating rate of 20 °C min^{-1}. Powder X-ray diffraction was performed on a D8 Advance diffractometer from Bruker and corrected for the background due to the sample holder.

Synthesis

2,5-dimethoxy-3,6-bis(thiophene-2-yl)-cyclohexa-2,5-diene-1,4-dione. A mixture of 1.00 g of 2,5-dibromo-3,6-dimethoxy-cyclohexa-2,5-diene-1,4-dione (3.07 mmol, 1.00 eq), 2.10 mL of 2-(tributylstannyl)thiophene (6.61 mmol, 2.15 eq) and 100 mg of $Pd(PPh_3)_4$ (0.09 mmol, 3%) and 100 mL of dry toluene were stirred and heated under reflux overnight under argon atmosphere. The reaction mixture was then filtered through celite®, which was washed with CH_2Cl_2 (around 30 mL) to recover the precipitated product and the solution was removed under reduced pressure. The crude was then purified by flash column chromatography (CH_2Cl_2:PE → CH_2Cl_2) to obtain the pure product as a brown-red crystalline powder in 95% yield. The crude could be also purified by recrystallization in hot MeOH affording high purity product with 82% yield. ^{1}H NMR (300 MHz, $CDCl_3$) δ 8.09 (dd, J = 3.9, 1.1 Hz, 1H), 7.55 (dd, J = 5.2, 1.1 Hz, 1H), 7.16 (dd, J = 5.2, 3.9 Hz, 1H), 4.15 (s, 3H). HR-MS (MALDI-TOF): 322.0184 ($[M]^-$, $C_{16}H_{12}O_4S_2$; calc 332.0177).

2,5-dihydroxy-3,6-bis(thiophene-2-yl)cyclohexa-2,5-diene-1,4-dione. To a dispersion of 2,5-dimethoxy-3,6-bis(thiophene-2-yl)-cyclohexa-2,5-diene-1,4-dione (850 mg, 2.54 mmol, 1 eq) in 150 mL of CH_3CN, 210 mg of NaOH (5.25 mmol, 2.06 eq) in 150 mL water was added under air.

The mixture was stirred and refluxed 2 h affording a dark blue-purple solution; this solution was filtered and slowly acidified with HCl 37% leading to a colour change to brown and formation of a brown crystalline precipitate. The solvent was then removed under reduced pressure and the brown product, dispersed in water, was filtered and washed with minimum amount of fresh CH_3CN one time and fresh water three times. The solid was then dried under air affording the product as a brown microcrystalline powder in 85% yield. ^{1}H NMR (300 MHz, Acetone-d6) δ 8.11 (dd, *J* = 3.9, 1.1 Hz, 1H), 7.62 (dd, *J* = 5.2, 1.1 Hz, 1H), 7.18 (dd, *J* = 5.2, 3.9 Hz, 1H); ESI-MS $[M-H]^-$: 303.0. IR-ATR: 3292(vs), 2953(w), 2921(m), 2851(w), 1630(vs), 1613(s), 1540(w), 1508(w), 1460(w), 1428(w), 1377(w), 1331(vs), 1292(vs), 1217(vs), 1100(w), 1067(w), 1050(w), 985(s), 911(w), 851(m), 838(m) 787(m), 750(m), 692(vs), 662(s), 618(s), 562(m), 492(w), 471(s).

[((HB(pz)$_3$)$_2$Dy)$_2$(μ-Th$_2$An)] (1Dy). $KHB(pz)_3$ 50.5 mg (0.2 mmol) was dissolved in 3 mL of $EtOH/CH_2Cl_2$ and added dropwise to a stirred solution of 45.6 mg of $Dy(NO_3)_3$*$6H_2O$ (0.1 mmol) in 5 mL of CH_2Cl_2 and 0.5 mL of EtOH, affording a fine white precipitate. After 5 min of stirring, a blue solution of deprotonated anilate ligand (15.2 mg, 0.05 mmol) of th$_2$An dissolved in 5 mL of CH_2Cl_2 and 15 mL of triethylamine was added and stirred for 10 minutes, affording a green solution with some white fine precipitate. The solution was filtered through celite and let in a glass crystallizer capped with aluminium foil for two days, giving after slow evaporation green prismatic crystals that were filtered under vacuum with a glass frit (95% yield, 87.3 mg). A crystal was maintained in contact with the mother liquor and transferred to silicon oil for SCXRD measurement. PXRD was performed on freshly filtered and gently grinded crystals to avoid solvent loss. MS(MALDI) $[M]^+$: 1479.2; $[M+Na]^+$: 1502.2; $[M+K]^+$ 1518.2. UV-Vis (DCM 5 × 10^{-6} M solution, λ_{max}/nm (ε/ L mol^{-1} cm^{-1})): 229 (8256), 267 (4316), 303 (5186), 316 (7484), 331 (10514), 348 (9094), 433 (2318), 706 (64). IR-ATR: 2457(w), 1496(vs),1433(w), 1403(m), 1385(m), 1363(m), 1298(s), 1212(s), 1198(m), 1119(s), 1066(w), 1045(vs), 1003(w), 975(w), 924(s), 884(w), 852(w), 829(w), 805(w), 777(w), 755(s), 735(w), 720(vs), 694(w), 665(m), 619(m), 566(w), 550(w), 481(m). Elemental analysis calc. for $C_{50}H_{46}B_4Dy_2N_{24}O_4S_2$*: C (40.59%), H (3.13%), N (22.72%), S (4.33%); found: C (40.38%), H (3.04%), N (22.37%), S (4.33%). *Calculated for fully desolvated form of the complex

[((HB(pz)$_3$)$_2$Dy)$_2$(μ-ClCNAn)] (2Dy). $KHB(pz)_3$ 50.5 mg (0.2 mmol) was dissolved in 3 mL of $EtOH/CH_2Cl_2$ and added dropwise to a stirred solution of 45.6 mg of $Dy(NO_3)_3 \cdot 6H_2O$ (0.1 mmol)

in 5 mL of CH_2Cl_2 and 0.5 mL of EtOH, affording a fine white precipitate. After 5 min of stirring, a red suspension of anilate ligand (11.5 mg, 0.05 mmol) KHClCNAn in 5 mL of CH_2Cl_2, 1 mL of EtOH and 15 mL of triethylamine was added and stirred for 1 h, affording a purple solution with some fine precipitate. The solution was filtered through celite and let in a glass crystallizer capped with aluminium foil for two days, giving after slow evaporation purple prismatic crystals that were filtered under vacuum, with a glass frit (45% yield, 34.6 mg). A crystal was maintained in contact with the mother liquor and transferred to silicon oil for SCXRD measurement. PXRD was performed on freshly filtered and gently grinded crystals to avoid solvent loss. MALDI-MS $[M-CN]^+$: 1346.2; $[M+2EtOH+Na]^+$ 1492.2. UV-Vis (CH_2Cl_2 5×10^{-6} M solution, λ_{max}/nm (e/ L mol^{-1} cm^{-1})): 229 (11090), 252 (3758), 260 (3734), 334 (9386), 345 (9798), 537 (134). IR-ATR: 2470(w), 2223(w), 1542(vs), 1523(s), 1504(s), 1433(w), 1422(w), 1404(m), 1386(m), 1299(s), 1267(w), 1212(s), 1199(m), 1119(s), 1066(w), 1048(vs), 1020(w) 979(m), 924(w), 895(w), 866(w), 806(w), 779(w), 764(vs), 755(s), 736(m), 720(vs), 663(m), 619(s), 583(w), 477(w), 452(m). Elemental analysis calc. for $C_{45}H_{44}B_4Cl_5Dy_2N_{25}O_4$: C (34.99%), H (2.87%), N (22.67%); found: C (34.96%), H (2.73%); N (22.40%).

X-ray diffraction measurements

X-ray single crystal diffraction data for **1Dy** and **2Dy** were collected at 100 K on a Bruker D8 Venture diffractometer (Mo Kα) equipped with a PHOTON II area detector. The data were indexed and processed with APEX3. The structures were solved by intrinsic phasing with SHELXT program[36] and refined on F^2 by full matrix least-squares algorithm using ShelXL[37] and Olex2.[38] All non-hydrogen atoms were refined anisotropically except the cyano residue in **2Dy**. All hydrogen atoms were placed in calculated positions and refined isotropically with a riding model. In the case of **1Dy** disordered water inside the voids was modelled through solvent mask implemented on Olex2. A summary of the crystallographic data and the structure refinement is given in Table 4.

Table 4 Crystallographic data of compounds 1Dy and 2Dy.

	1Dy	**2Dy**
Empirical formula	$C_{27}H_{27}B_2Cl_4DyN_{12}O_2S$	$B_{1.33}C_{14.33}Cl_{0.33}Dy_{0.67}N_{8.33}O_{2.67}H_{0.17}$
Formula weight	1851.60	1544.54

Temperature/K	102.00	100.00
Crystal system	Tetragonal	monoclinic
Space group	$P4_2/n$	$P2_1/n$
a/Å	17.5240(13)	14.0640(9)
b/Å	17.5240(13)	14.9703(9)
c/Å	23.4960(17)	14.7616(9)
α/°	90	90
β/°	90	107.819(2)
γ/°	90	90
Volume/Å^3	7215.4(12)	2958.8(3)
Z	4	2
ρ_{calc}g/cm^3	1.704	1.734
μ/mm^{-1}	2.474	2.797
F(000)	3664.0	1516.0
Crystal size/mm^3	0.19 × 0.08 × 0.08	0.25 × 0.16 × 0.06
Radiation	MoKα (λ = 0.71073)	MoKα (λ = 0.71073)
2Θ range for data collection/°	3.716 to 52.116	4.434 to 65.652
Index ranges	$-21 \leq h \leq 21$, $-21 \leq k \leq 21$, $-28 \leq l \leq 29$	$-20 \leq h \leq 20$, $-22 \leq k \leq 22$, $-19 \leq l \leq 22$
Reflections collected	54728	80706
Independent reflections	7142 [R_{int} = 0.0795, R_{sigma} = 0.0436]	9875 [R_{int} = 0.0758, R_{sigma} = 0.0509]
Data/restraints/parameters	7142/0/450	9875/1/405
Goodness-of-fit on F^2	1.029	1.080
Final R indexes [I>=2σ (I)]	R_1 = 0.0307, wR_2 = 0.0691	R_1 = 0.0328, wR_2 = 0.0743
Final R indexes [all data]	R_1 = 0.0435, wR_2 = 0.0761	R_1 = 0.0590, wR_2 = 0.0885
Largest diff. peak/hole / e Å^{-3}	0.63/-0.73	1.73/-2.19
CCDC numbers	2324974	2324975

Electrochemical studies

Cyclic voltammetry measurements were performed with a SP150 Biologic Potentiostat inside a N_2 filled glovebox at 298 K using dry and degassed solvent, a 0.5 mM solution in CH_2Cl_2 for th2An, **1Dy**, **2Dy**, and 0.5 mM solution in CH_3CN for KHClCNAn. A three-electrode configuration was

used: a 2 mm platinum disk as working electrode (WE), platinum wire as counter electrode (CE) and Ag wire as pseudoreference electrode (RE) in 0.25 M $TBAPF_6$ as supporting electrolyte, with a scan rate of 100 $mV \cdot s^{-1}$. Cathodic and anodic regions were scanned separately; all potentials are referred relative to $Fc^{0/+}$ internal standard.

Magnetic measurements

Magnetic measurements were carried out on polycrystalline samples of **1Dy** and **2Dy** with a Quantum Design MPMS-XL-7T SQUID magnetometer (Quantum Design, Inc, San Diego, CA, USA). Magnetic measurements (dc) were carried out under an applied field of 1000 Oe. ac susceptibility measurements were carried out with an alternating magnetic field of 3.95 Oe, in the 1-1500 Hz frequency range, and under an external applied field in the range 0-1500 Oe.

Computational details

Wavefunction-based calculations were carried out on the molecular structures of **1Dy** and **2Dy** complexes by using the SA-CASSCF/RASSI-SO approach, as implemented in the OpenMolcas quantum chemistry package (versions 22.10).[39] Calculations were performed on each Dy^{III} centre, with the second Dy^{III} centre replaced by the closed-shell Y^{III} ion. Relativistic effects are treated in two steps on the basis of the Douglas–Kroll Hamiltonian. First, the scalar terms were included in the basis-set generation and were used to determine the spin-free wavefunctions and energies in the complete active space self-consistent field (CASSCF) method.[40] Next, spin-orbit coupling was added within the restricted-active-space-state-interaction (RASSI-SO) method, which uses the spin-free wavefunctions as basis states.[41] Spin−orbit (SO) integrals are calculated using the AMFI (atomic mean- field integrals) approximation.[42] The resulting wavefunctions and energies are used to compute the magnetic properties and g-tensors of the lowest states from the energy spectrum by using the pseudo-spin S = 1/2 formalism in the SINGLE-ANISO routine.[43] Cholesky decomposition of the bielectronic integrals was employed to save disk space and speed-up the calculations.[44] Dipole-dipole magnetic couplings between the Dy centres were obtained using the POLY_ANISO routine.[45] The active space consisted of the nine 4f electrons of the Dy^{III} ion spanning the seven 4f orbitals, i.e. CAS(9,7)SCF. State-averaged CASSCF calculations were performed for all of the sextets (21 roots), all of the quadruplets (224 roots), and 300 out of the 490 doublets of the Dy^{III} ion. 21 sextets, 128 quadruplets, and 107 doublets were mixed through

spin−orbit coupling in RASSI-SO. All atoms were described by ANO-RCC basis sets.[46] The following contractions were used: [8s7p4d3f2g1h] for Dy, [7s6p4d2f] for Y, [4s3p1d] for O and N, [4s3p] for S, [3s2p] for C and B and [2s] for H. The atomic positions were extracted from the X-ray crystal structures. Only the positions of the H atoms were optimized with the AMS program suite (revision 2022.103).[47] These calculations utilized the scalar all-electron zeroth-order regular approximation (ZORA) along with the revPBE (Perdew-Burke-Ernzerhof) functional.[48] For all atoms, the atomic basis set corresponded to the triple-ζ polarized (TZP) Slater-type orbital (STO) all-electron basis set.[49]

ORCID

Fabio Manna: 0009-0002-5246-1952

Mariangela Oggianu: 0000-0002-6579-4492

José Ramón Galán-Mascarós: 0000-0001-7983-9762

Flavia Pop: 0000-0003-3524-9781

Boris Le Guennic: 0000-0003-3013-0546

Maria Laura Mercuri: 0000-0002-4816-427X

Narcis Avarvari: 0000-0001-9970-4494

Conflicts of interest

There are no conflicts of interest to declare.

Acknowledgements

This work was supported in France by the CNRS and the University of Angers. This research was funded in Italy by Fondazione di Sardegna, Convenzione Triennale tra la Fondazione di Sardegna e gli Atenei Sardi, Regione Sardegna, L.R. 7/2007 annualità 2022, project VOC_3D "*3D printed optical VOC sensors for indoor air quality evaluation*" CUP F73C23001590007. CeSAR (Centro Servizi d'Ateneo per la Ricerca) *core* facility of the University of Cagliari, Italy, is also acknowledged for SCXRD analyses. J.R.G.M. acknowledges the support from MCIN/AEI/10.13039/501100011033/ through project PID2021-124796OB-I00 and from the

Generalitat de Catalunya (2021SGR1154). ICIQ is supported by the Ministerio de Ciencia e Innovación through the Severo Ochoa Excellence Accreditations CEX2019-000925-S (MCIN/AEI) and CEX2021-001214-S and by the CERCA Programme/Generalitat de Catalunya. B.L.G. thanks the French GENCI/IDRIS-CINES centres for high-performance computing resources.

Notes and references

1 M. A. Novak, R. Sessoli, D. Gatteschi and A. Caneschi, *Nature*, 1993, **365**, 141–143.

2 R. Sessoli, H. Tsai, A. R. Schake, S. Wang, J. B. Vincent, K. Foiling, D. Gatteschi, G. Christou, D. N. Hendrickson, L. Jolla, D. Chimica and U. Firenze, *J. Am. Chem. Soc*. 1993, 115, 1804–1816.

3 T. G. Ashebr, H. Li, X. Ying, X. L. Li, C. Zhao, S. Liu and J. Tang, *ACS Mater. Lett.*, 2022, **4**, 307–319.

4 J. D. Rinehart and J. R. Long, *Chem. Sci.*, 2011, **2**, 2078–2085.

5 F. Manna, M. Oggianu, N. Avarvari and M. L. Mercuri, *Magnetochemistry*, 2023, *9*, 190,

6 F. Tuna, C. A. Smith, M. Bodensteiner, L. Ungur, L. F. Chibotaru, E. J. L. McInnes, R. E. P. Winpenny, D. Collison and R. A. Layfield, *Angew. Chemie - Int. Ed.*, 2012, 51, 6976–6980.

7 S. Demir, I. R. Jeon, J. R. Long and T. D. Harris, *Coord. Chem. Rev.*, 2015, 289–290, 149–176.

8 H. D. Li, S. G. Wu and M. L. Tong, *Chem. Commun.*, 2023, 59, 6159–6170.

9 K. Martyanov and V. Kuropatov, *Inorganics*, 2018, 6, 48–76.

10 M. L. Mercuri, F. Congiu, G. Concas and S. A. Sahadevan, 2017, *3*, 17.

11 S. Benmansour and C. J. Gómez-García, *Magnetochemistry*, 2020, **6**, 1–44.

12 S. Kitagawa and S. Kawata, *Coord. Chem. Rev.*, 2002, **224**, 11–34.

13 J. A. DeGayner, I. R. Jeon, L. Sun, M. Dincă and T. D. Harris, *J. Am. Chem. Soc.*, 2017, **139**, 4175–4184.

14 N. Monni, M. S. Angotzi, M. Oggianu, S. A. Sahadevan and M. L. Mercuri, *J. Mater. Chem. C*, 2022, **10**, 1548–1572.

15 N. Monni, M. Oggianu, S. A. Sahadevan and M. L. Mercuri, *Magnetochemistry*, , **2021**, *7*, 109.

16 M. Oggianu, A. Abhervé, D. Marongiu, F. Quochi, J. R. Galán-Mascarós, F. Bertolotti, N. Masciocchi, N. Avarvari and M. L. Mercuri, *Molecules*, *Molecules* **2023**, *28*, 6453

17 S. Ashoka Sahadevan, N. Monni, M. Oggianu, A. Abhervé, D. Marongiu, M. Saba, A. Mura, G. Bongiovanni, V. Mameli, C. Cannas, N. Avarvari, F. Quochi and M. L. Mercuri, *ACS Appl. Nano Mater.*, 2020, **3**, 94–104.

18 S. Ashoka Sahadevan, F. Manna, A. Abhervé, M. Oggianu, N. Monni, V. Mameli, D. Marongiu, F. Quochi, F. Gendron, B. Le Guennic, N. Avarvari and M. L. Mercuri, *Inorg. Chem.*, 2021, **60**, 17765–17774.

19 S. A. Sahadevan, N. Monni, A. Abhervé, G. Cosquer, M. Oggianu, G. Ennas, M. Yamashita, N. Avarvari and M. L. Mercuri, *Inorg. Chem.*, 2019, **58**, 13988–13998.

20 S. Ashoka Sahadevan, N. Monni, A. Abhervé, D. Marongiu, V. Sarritzu, N. Sestu, M. Saba, A. Mura, G. Bongiovanni, C. Cannas, F. Quochi, N. Avarvari and M. L. Mercuri, *Chem. Mater.*, 2018, **30**, 6575–6586.

21 S. A. Sahadevan, A. Abhervé, N. Monni, C. Sáenz De Pipaón, J. R. Galán-Mascarós, J. C. Waerenborgh, B. J. C. Vieira, P. Auban-Senzier, S. Pillet, E. E. Bendeif, P. Alemany, E. Canadell, M. L. Mercuri and N. Avarvari, *J. Am. Chem. Soc.*, 2018, **140**, 12611–12621.

22 T. Han, J. B. Petersen, Z. H. Li, Y. Q. Zhai, A. Kostopoulos, F. Ortu, E. J. L. McInnes, R. E. P. Winpenny and Y. Z. Zheng, *Inorg. Chem.*, 2020, **59**, 7371–7375.

23 A. E. Thorarinsdottir, R. Bjornsson and T. David Harris, *Inorg. Chem.*, 2020, **59**, 4634–4649.

24 M. Abdus Subhan, R. Kawahata, H. Nakata, A. Fuyuhiro, T. Tsukuda and S. Kaizaki, *Inorganica Chim. Acta*, 2004, **357**, 3139–3146.

25 R. Ishikawa, S. Michiwaki, T. Noda, K. Katoh, M. Yamashita, K. Matsubara and S. Kawata, *Inorganics*, 2018, **6**, 1–13.

26 M. A. Dunstan, E. Rousset, M. E. Boulon, R. W. Gable, L. Sorace and C. Boskovic, *Dalt. Trans.*, 2017, **46**, 13756–13767.

27 W. R. Reed, M. A. Dunstan, R. W. Gable, W. Phonsri, K. S. Murray, R. A. Mole and C. Boskovic, *Dalt. Trans.*, 2019, **48**, 15635–15645.

28 P. Zhang, M. Perfetti, M. Kern, P. P. Hallmen, L. Ungur, S. Lenz, M. R. Ringenberg, W. Frey, H. Stoll, G. Rauhut and J. Van Slageren, *Chem. Sci.*, 2018, **9**, 1221–1230.

29 R. Ishikawa, S. Michiwaki, T. Noda, K. Katoh, M. Yamashita and S. Kawata, *Magnetochemistry*, 2019, **5**, 30–42.

30 M. Atzori, F. Pop, T. Cauchy, M. L. Mercuri and N. Avarvari, *Org. Biomol. Chem.*, 2014, **12**, 8752–8763.

31 M. Atzori, F. Artizzu, L. Marchiò, D. Loche, A. Caneschi, A. Serpe, P. Deplano, N. Avarvari and M. L. Mercuri, *Dalt. Trans.*, 2015, **44**, 15786–15802.

32 Llunell, M.; Casanova, D.; Girera, J.; Alemany, Alvarez, S. SHAPE, version 2.1; Universitat de Barcelona: Barcelona, Spain.

33 S. Alvarez, P. Alemany, D. Casanova, J. Cirera, M. Llunell and D. Avnir, *Coord. Chem. Rev.*, 2005, **249**, 1693–1708.

34 N. G. Connelly and W. E. Geiger, *Chem. Rev.*, 1996, **96**, 877–910.

35 X. Gan, W. Jiang, W. Wang and L. Hu, *Org. Lett.*, 2009, **11**, 589–592.

36 G. M. Sheldrick, *Acta Crystallogr. Sect. A Found. Crystallogr.*, 2015, **71**, 3–8.

37 G. M. Sheldrick, *Acta Crystallogr. Sect. C Struct. Chem.*, 2015, **71**, 3–8.

38 O. V. Dolomanov, L. J. Bourhis, R. J. Gildea, J. A. K. Howard and H. Puschmann, *J. Appl. Crystallogr.*, 2009, **42**, 339–341.

39 I. F, Galván, M. Vacher, A. Alavi, C. Angeli, F. Aquilante, J. Autschbach, J. J. Bao, S. I. Bokarev, N. A. Bogdanov, R. K. Carlson, L. F. Chibotaru, J. Creutzberg, N. Dattani, M. G. Delcey, S. S. Dong, A. Dreuw, L. Freitag, L. M. Frutos, L. Gagliardi, F. Gendron, A. Giussani, L. González, G. Grell, M. Guo, C. E. Hoyer, M. Johansson, S. Keller, S. Knecht, G. Kovačević, E. Källman, G. Li Manni, M. Lundberg, Y. Ma, S. Mai, J. P. Malhado, P. Å. Malmqvist, P. Marquetand, S. A. Mewes, J. Norell, M. Olivucci, M. Oppel, Q. M. Phung, K. Pierloot, F. Plasser, M. Reiher, A. M. Sand, I. Schapiro, P. Sharma,C. J. Stein, L. K. Sørensen, D. G. Truhlar, M. Ugandi, L. Ungur, A. Valentini, S. Vancoillie, V. Veryazov, O. Weser, T. A. Wesołowski,P.-O. Widmark, S. Wouters, A. Zech, J. P. Zobel and R. Lindh, *J. Chem. Theory Comput*. 2019, **15**, 5925–5964.

40 B. O. Roos, P. R. Taylor and P. E. M. Siegbahn, *Chem. Phys.*, 1980, **48**, 157–173.

41 a) P.-A. Malmqvist, B. O. Roos and B. Schimmelpfennig, *Chem. Phys. Lett.*, 2002, **357**, 230–240. b) P.-A. Malmqvist and B. O. Roos, *Chem. Phys. Lett.*, 1989, **155**, 189–194.

42 B. A. Heß, C. M. Marian, U. Wahlgren and O. Gropen, *Chem. Phys. Lett.*, 1996, **251**, 365–371.

43 a) L. F. Chibotaru and L. Ungur, *J. Chem. Phys.*, 2012, **137**, 064112. b) L. F. Chibotaru, L. Ungur and A. Soncini, *Angew. Chem. Int. Ed.*, 2008, **47**, 4126–4129.

44 F. Aquilante, P.-A. Malmqvist, T. B. Pedersen, A. Ghosh and B. O. Roos, *J. Chem. Theory Comput.*, 2008, **4**, 694–702.

45 a) L. F. Chibotaru, L. Ungur and A. Soncini, *Angew. Chem. Int. Ed.*, 2008, **120**, 4194–4197. b) L. Ungur, W. V. den Heuvel, and L. F. Chibotaru, *New J. Chem.*, 2009, **33**, 1224–1230.

46 a) B. O. Roos, R. Lindh, P.-A. Malmqvist, V. Veryazov and P.-O. Widmark, *J. Phys. Chem. A*, 2004, **108**, 2851–2858. b) B. O. Roos, R. Lindh, P.-A. Malmqvist, V. Veryazov, P.-O. Widmark and A.-C. Borin, *J. Phys. Chem. A*, 2008, **112**, 11431–11435.

47 a) G. te Velde, F. M. Bickelhaupt, E. J. Baerends, C. Fonseca Guerra, S. J. A. van Gisbergen, J. G. Snijders and T. Ziegler, *J. Comp. Chem.*, 2001, **22**, 931–967. b) AMS 2022.103, Amsterdam, The Netherlands, http://www.scm.com.

48 J. P. Perdew, K. Burke and M. Ernzerhof, *Phys. Rev. Lett.*, 1997, **78**, 1396.

49 E. Van Lenthe and E. J. Baerends, *J. Comput. Chem.*, 2003, **24**, 1142–1156.